

# Electronic structure and magnetic properties of the graphene/Ni<sub>3</sub>Mn/Ni(111) trilayer

Elena Voloshina,<sup>1,2,\*</sup> Qilin Guo,<sup>1,2</sup> Beate Paulus,<sup>2</sup> Stefan Böttcher,<sup>3</sup>  
Karsten Horn,<sup>3</sup> Changbao Zhao,<sup>4,5</sup> Yi Cui,<sup>4,†</sup> and Yuriy Dedkov<sup>1,‡</sup>

<sup>1</sup>*Department of Physics, Shanghai University, 99 Shangda Road, 200444 Shanghai, China*

<sup>2</sup>*Freie Universität Berlin, Physikalische und Theoretische Chemie, 14195 Berlin, Germany*

<sup>3</sup>*Fritz Haber Institut of the Max Planck Society, 14195 Berlin, Germany*

<sup>4</sup>*Vacuum Interconnected Nanotech Workstation,*

*Suzhou Institute of Nano-Tech and Nano-Bionics,*

*Chinese Academy of Sciences, 215123 Suzhou, China and*

<sup>5</sup>*Nano Science and Technology Institute,*

*University of Science and Technology of China, 215123 Suzhou, China*

(Dated: April 21, 2022)

---

\* Corresponding author. E-mail: voloshina@shu.edu.cn

† Corresponding author. E-mail: ycui2015@sinano.ac.cn

‡ Corresponding author. E-mail: dedkov@shu.edu.cn

## Abstract

Experimental and theoretical studies of manganese deposition on graphene/Ni(111) shows that a thin ferromagnetic Ni<sub>3</sub>Mn layer, which is protected by the graphene overlayer, is formed upon Mn intercalation. The electronic bands of graphene are affected by Ni<sub>3</sub>Mn interlayer formation through a slight reduction of *n*-type doping compared to graphene/Ni(111) and a suppression of the interface states characteristic of graphene/Ni(111). Our DFT-based theoretical analysis of interface geometric, electronic, and magnetic structure gives strong support to our interpretation of the experimental scanning tunneling microscopy, low energy electron diffraction, and photoemission results, and shows that the magnetic properties of graphene on Ni(111) are strongly influenced by Ni<sub>3</sub>Mn formation.

This document is the unedited author's version of a Submitted Work that was subsequently accepted for publication in J. Phys. Chem. C., copyright © American Chemical Society after peer review. To access the final edited and published work see doi: 10.1021/acs.jpcc.9b00942.

## I. INTRODUCTION

Recently, graphene-metal interfaces have attracted a lot of attention [1, 2] because many promising ideas of technological applications of these systems have appeared in the literature. For example, the synthesis of large layers of high-quality graphene (gr) on metals [3–5] is considered as the most promising method, which in future may be implemented in different areas of micro-electronics and nano-technology [6, 7]. Also, graphene is found to be one of the best one-atom-thick protection layers for different substrates, metallic as well as semiconducting [8–14].

Considering the electronic structure of graphene-metal systems, graphene on these substrates always becomes either  $n$  or  $p$  doped, demonstrating, in some cases, also the overlap of the graphene  $\pi$  states and valence band states of the underlying material (space-, energy-, and  $k$ -vector-overlapping). Such cases are described as *strongly* interacting graphene with metals [15, 16]. In graphene/metal system belonging to this group, the electronic structure of graphene is heavily disturbed due to the above mentioned overlap of the valence band states of graphene and metal, leading to the loss of the free-standing character of the electronic structure in graphene.

Among the *strongly* interacting systems, the graphene-ferromagnet (gr-FM) interfaces are the most exciting due to their perspectives for spintronic applications. For example, it was predicted that a stack of graphene layers can be used as an effective spin filter in FM-gr $_n$ -FM sandwiches [17, 18]. The overlap of the valence band states of graphene and the FM material drastically reduces spin-filtering effect for the single graphene layer, which however can be improved via placing layers of noble metals or h-BN between graphene and the FM [18, 19]. However, the overlap of the electronic states at the interface between graphene and FM materials (Ni, Co) allows to observe the induced spin-polarization of the graphene  $\pi$  states that was confirmed in a series of spectroscopic experiments for gr/Ni(111) and gr/Co(0001) [20–24] and this effect can be used for an effective spin injection and manipulation in graphene.

The electronic structure of the gr-FM interface can be tailored via intercalation of different species with the aim to prepare different graphene-based heterostructures. Here, e. g., the intercalation of Fe leads to an increase of the induced magnetic moment in graphene [22], the intercalation of  $sp$ -metals decouples graphene from the FM with the controllable modification

of the graphene band structure around the Dirac point [25–28]. The intercalation of oxygen leads to the formation of thin layers of oxides and the resulting epitaxial systems might be used in future spintronics applications [29, 30]. Moreover, the insertion of other magnetic atoms with open  $d$ -shells into the gr-FM interface might lead to the formation of ordered gr/FM-alloy systems with interesting properties.

Here we present systematic electronic structure studies of the system formed after intercalation of Mn in gr/Ni(111). It is found that an ordered ( $2 \times 2$ ) structure with respect to gr/Ni is formed at the interface, indicating the formation of a thin layer of the strong FM Ni<sub>3</sub>Mn alloy. This alloy is effectively protected by a graphene monolayer and the electronic structure of this system was studied via application of different spectroscopic methods, accompanied by theoretical calculations. Very good agreement is found between theory and experiment.

## II. RESULTS AND DISCUSSION

*LEED and STM.* The intercalation of Mn atoms in gr/Ni(111) and formation of the intercalation-like systems was studied in a series of experiments using STM, LEED and XPS. Fig. 1 shows large and small scale STM images of gr/Ni(111) (a,b) and of the system obtained after annealing of Mn/gr/Ni(111) at 400° C (c-e). The respective LEED images of the studied systems are presented as insets for large scale STM data. Due to the lattice match of graphene and Ni(111) (the difference is approximately 1%), LEED and STM of the gr/Ni(111) system demonstrate ( $1 \times 1$ ) in-plane periodicities indicating also the high quality of this system on the large and the atomic scale. The number of defects in the graphene layer for this system is very small; however, some areas associated with the presence of the Ni<sub>2</sub>C phase (small scale STM images of this area are not shown here) can be detected on the surface; this is also supported by the XPS data and consistent with the previously published results for the same system [30–32]. The LEED and STM images of the system obtained after intercalation of Mn in gr/Ni(111) demonstrate ( $2 \times 2$ ) periodicities with respect to the ones of the parent system (Fig. 1). Small scale STM images presented in (d) and (e) were collected at slightly different bias voltages that might cause the change in the imaging contrast. Fast Fourier transformation (FFT) images of the atomically resolved STM data for gr/Ni(111) before and after intercalation of Mn are shown in panels (f) and (g), respectively,

with the extracted corresponding intensity profiles shown in (h), and they also confirm the formation of a  $(2 \times 2)$  structure for the gr-Mn-Ni(111) interface.

*XPS and NEXAFS.* Figure 2 compiles the results of the XPS studies: (a) survey spectra before and after Mn intercalation in gr/Ni(111) and the respective core-level spectra, (b) Ni  $2p$ , (d) Mn  $2p$ , and (f) C  $1s$ . The corresponding NEXAFS spectra are shown on the right-hand side: (c) Ni  $L_{2,3}$ , (e) Mn  $L_{2,3}$ , and (g)  $CK$ . The process of Mn intercalation is characterized by the corresponding intensity variations of XPS lines as well as line shape modifications for the C  $1s$  and Mn  $2p$  lines.

For the gr/Ni(111) system the binding energy of the C  $1s$  line is  $284.95 \pm 0.05$  eV, which is in good agreement with previously measured values [20]. The higher binding energy for this line compared to the neutral graphene (284.1 eV [33]) indicates the strong  $n$  doping of graphene in the former case. After intercalation of Mn in gr/Ni(111) the intensity of the C  $1s$  line is almost fully restored and a small energy shift of this line of  $\approx 140$  meV to smaller binding energies is detected indicating a small reduction of  $n$ -doping of the graphene layer.

Intercalation of Mn in gr/Ni(111) leads to a slight broadening of both Mn spin-orbit split peaks compared to the Mn  $2p$  XPS spectra for the non-intercalated case. This increase of the width of the Mn  $2p_{3/2,1/2}$  emission lines as well as the previously observed  $(2 \times 2)$  structures in LEED and STM data can be assigned to the formation of a thin layer of Ni<sub>3</sub>Mn alloy at the gr/Mn-Ni(111) interface [34–37]. The formation of the NiMn phase can be ruled out as it would show  $p(2 \times 1)$  patterns for the single domain and  $(2 \times 2)$  patterns from all possible three fold rotated domains; however, a  $p(2 \times 1)$  structure was not observed in the STM experiments, which reflect the local (domain) structure (see Fig. 1). In the XPS spectra one can assign the broadening of the Mn  $2p$  lines to the appearance of emission satellites (marked by arrows in (d)). We believe that the increased Mn-Mn distance in the Ni<sub>3</sub>Mn(111) plane compared to bulk Mn leads to an increase of the Mn  $3d - 3d$  correlations and a slightly reduced screening for the core hole as seen in other systems [34, 36, 37]. The same is valid for the description of the Mn  $L_{2,3}$  NEXAFS spectra where additional weak correlation satellites are visible at  $\approx 640$  eV and  $\approx 647.5$  eV (marked by arrows) (see Fig. 2(e) and Refs. 34, 37).

The  $CK$  NEXAFS spectra obtained for gr/Ni(111) measured in the PEY and TEY modes (Fig. 2(g), red dashed and solid curves, respectively) are in very good agreement with previously published data [20, 38–40]. Two structures in the ranges 284 – 288 eV and 289.5 – 294.5 eV are assigned to the  $1s \rightarrow \pi^*$  and  $1s \rightarrow \sigma^*$  transitions, respectively. A

closeup analysis of the NEXAFS spectra of gr/Ni(111) and gr/Ni<sub>3</sub>Mn/Ni(111) shows that the  $1s \rightarrow \pi^*$  absorption edge for the latter system is shifted to smaller photon energies by  $\approx 300$  meV and the energy separation between the peaks of  $\pi^*$  and  $\sigma^*$  features is increased by  $\approx 430$  meV (the respective peak shifts are marked in (g)). This effect is assigned to the reduced  $n$ -doping of a graphene layer and its slightly smaller buckling as previously discussed [28, 38].

*ARPES.* Figure 3 shows ARPES intensity maps measured for (a) gr/Ni(111) and (b) gr/Ni<sub>3</sub>Mn/Ni(111) at a photon energy of  $h\nu = 63$  eV. The corresponding intensity profiles taken at the  $\Gamma$  and K points of the graphene-derived BZ are presented in panels (c) and (d), respectively. Compared to free-standing graphene, the electronic structure of graphene on Ni(111) is strongly modified due to the  $n$ -doping and a strong spatial and energy overlap of the graphene  $\pi$  and Ni  $3d$  valence band states. As a result, the states of graphene are shifted to higher binding energies and the bottom of the  $\pi$  band is found at  $E - E_F = -9.98 \pm 0.01$  eV at the  $\Gamma$  point, consistent with previously published data [21, 28, 30, 40] (Fig. 3(c)). The overlap and hybridization of the valence band states of graphene and Ni leads to the formation of the so-called interface states below and above  $E_F$  [28, 41]; they can be clearly recognised as a series of peaks in the energy range  $E - E_F = 0 \dots -2.2$  eV in the intensity profile taken at the K point for gr/Ni(111) (Fig. 3(d)). The partial charge transfer from ferromagnetic Ni to graphene and hybridization between valence band states leads to the appearance of the magnetic moment of C atoms in graphene as confirmed in the experiment [20, 22, 39].

The intercalation of Mn in gr/Ni(111) followed by the formation of a thin layer of Ni<sub>3</sub>Mn leads to the shift of the graphene  $\pi$  band to smaller binding energy, indicating the slightly smaller  $n$ -doping of graphene compared to the parent system. The bottom of the  $\pi$  band at the  $\Gamma$  point in this case is located at  $E - E_F = -9.71 \pm 0.01$  eV, i.e. it is shifted by  $0.27 \pm 0.02$  eV to smaller binding energies (Fig. 3(c)). The electronic structure around the K point is also modified as manifested by the suppression of the strong intensity associated with the interface states found in the previous system (Fig. 3(d)).

Adsorption of graphene on Ni(111) strongly modifies the surface electronic structure of the Ni substrate and, as was shown, leads to the shift of the surface states of Ni(111) into the energy range above  $E_F$  [42]. The 2D ARPES intensity map for gr/Ni(111) (Fig. 4(a)) shows undressed surface projections of the Ni energy bands:  $d_{\downarrow}$  disperses from  $E - E_F = -1.4$  eV

at  $\Gamma$  to  $E_F$  at  $k_{\parallel} \approx 1 \text{ \AA}^{-1}$  and  $sp_{\downarrow}$  crosses  $E_F$  at  $k_{\parallel} \approx 1 \text{ \AA}^{-1}$  [43, 44]. After the formation of the thin layer of  $\text{Ni}_3\text{Mn}$  at the  $\text{gr}/\text{Ni}(111)$  interface, the electronic structure is modified as shown in Fig. 4(b): the intensity of the  $d_{\downarrow}$  band is suppressed and the  $sp_{\downarrow}$  is not present in the spectra. At the same time the intense bands at the  $\Gamma$  point, which can be assigned to the  $\text{Ni } 3d$  states or to the mixture of the  $\text{Ni}+\text{Mn } 3d$  bands, are shifted from  $E - E_F \approx -1.4 \text{ eV}$  for  $\text{gr}/\text{Ni}(111)$  to  $E - E_F \approx -1 \text{ eV}$  for  $\text{gr}/\text{Ni}_3\text{Mn}/\text{Ni}(111)$ , respectively [45, 46]. All these changes, which clearly demonstrate the occurrence of a new phase (i.e.  $\text{Ni}_3\text{Mn}$ ) as also shown by the structural data and discussed below, have implications on the electronic and transport properties of graphene in this system.

*DFT.* The experimental data were compared with the respective DFT results for the different Mn-intercalation  $\text{gr}/\text{Ni}(111)$  structures. The energetically most favourable structures after geometry optimization are presented in Fig. 5 (a-d). For the parent  $\text{gr}/\text{Ni}(111)$  system (Fig. 5 (a)) the so-called *top-fcc* configuration of C-atoms above  $\text{Ni}(111)$  is the most energetically favourable with a distance between a graphene layer and top Ni layer of  $2.09 \text{ \AA}$ . In case of 1 ML-Mn layer placed between graphene and  $\text{Ni}(111)$  the Mn-Mn distance is  $2.88 \text{ \AA}$ , which is by 5% large compared to the *fcc*  $\gamma$ -Mn stabilized on  $\text{Pd}(111)$  [47] (Fig. 5 (b)). For the next two systems, a graphene layer is placed either on 1 ML-thick  $\text{Ni}_3\text{Mn}$ -layer on  $\text{Ni}(111)$  (Fig. 5 (c)) or on a bulk layer of  $\text{Ni}_3\text{Mn}$  (Fig. 5 (d)). The equilibrium distances between graphene and the top metallic layer in all structures are (b)  $2.04 \text{ \AA}$ , (c)  $2.13 \text{ \AA}$ , and (d)  $2.12 \text{ \AA}$ , respectively.

Due to the small change of the distance between graphene and the underlying metallic support for all considered systems, before and after Mn intercalation in  $\text{gr}/\text{Ni}(111)$ , an electron transfer from the underlying metal on graphene is observed, leading to *n*-doped graphene in all cases (see  $\Delta\rho(r)$  maps in the side views of Fig. 5). Due to the fact that the Dirac cone in all systems is fully destroyed due to the hybridization of the graphene  $\pi$  and  $\text{Ni}(\text{Mn}) 3d$  states, the value of doping change after Mn intercalation in experimental and theoretical data can be compared with the shift of the position of the graphene  $\pi$  band at the  $\Gamma$  point measured for the systems before and after Mn intercalation in  $\text{gr}/\text{Ni}(111)$ . The calculated shifts of this band are  $0.48 \text{ eV}$  for  $\text{gr}/1 \text{ ML-Mn}/\text{Ni}(111)$  (Fig. 5(b)),  $0.18 \text{ eV}$  for  $\text{gr}/1 \text{ ML-Ni}_3\text{Mn}/\text{Ni}(111)$  (Fig. 5(c)), and  $0.24 \text{ eV}$  for  $\text{gr}/\text{Ni}_3\text{Mn}(111)$  (Fig. 5(d)), thus supporting our earlier conclusions about  $\text{Ni}_3\text{Mn}$  formation under the graphene layer.

The intercalation of Mn in  $\text{gr}/\text{Ni}(111)$  leads to changes of the magnetic configuration

in graphene layer compared to the parent system. The resulting magnetic moments of C atoms in the considered systems are presented in Tab. I (C1-C4 are referenced to marks in Fig. 5). For gr/1 ML-Mn/Ni(111), all magnetic moments in graphene are coupled antiferromagnetically with respect to the magnetization of the Ni(111) substrate, caused by the presence of the Mn layer at the interface. For the other two systems with Ni<sub>3</sub>Mn underneath a graphene layer, the configurations of magnetic moments in graphene are close to each other - magnetic moments of the C atoms are aligned parallel to the magnetization of the Ni(111) bulk or Ni<sub>3</sub>Mn, except for C1. However, it is interesting to note that the total absolute magnetization of graphene (ferromagnetically or antiferromagnetically coupled to Ni(111)) is increased for all Mn-intercalation systems compared to gr/Ni(111) allowing the effective spin manipulation in graphene which is in contact with such Ni-Mn interfaces.

Figures 6 and 7 show the calculated spin-resolved partial density of states for graphene  $\pi$  states and the spin-resolved band structure, respectively, for the systems: (a) gr/Ni(111), (b) gr/1 ML-Mn/Ni(111), (c) gr/1 ML-Ni<sub>3</sub>Mn/Ni(111), and (d) gr/bulk-Ni<sub>3</sub>Mn(111). For a more accurate comparison, the unit cell of gr/Ni(111) was modelled in the same ( $2 \times 2$ ) periodicity as for Mn-based interfaces. The calculated band structure for gr/Ni(111) is similar to the one presented in earlier works [22, 28] except for the folded bands originating from the doubled periodicity of the system.

Comparing our NEXAFS and ARPES experimental data with the presented band structures we can find a close similarity between experimental and theoretical band structures for gr/Ni(111) and gr/Ni<sub>3</sub>Mn/Ni(111). [In the present situation it is very difficult (if not impossible) to estimate from the experimental data the thickness of the Ni<sub>3</sub>Mn layer. However, the presented results (Fig. 7(c,d)) show that the electronic structures of both gr/Ni<sub>3</sub>Mn interfaces are very similar.] Intercalation of Mn and the formation of Ni<sub>3</sub>Mn underneath of a graphene layer lead to a small upward shift of the graphene-derived spin-up bands by  $\approx 100$  meV leaving the value of the gap between upper and lower branches of  $\approx 400$  meV almost unchanged. At the same time, the structure of the interface states for both spins between graphene and the metallic support becomes smeared in energy due to the hybridization between the respective valence band states of graphene and the Ni<sub>3</sub>Mn alloy. All these facts are in good agreement with experimental data where a smaller  $n$ -doping of graphene and suppression of the intensity of the interface states around the K point was observed.

Close analysis of the calculated band structure for gr/1 ML-Ni<sub>3</sub>Mn/Ni(111), which we

conclude to be formed in the present experiment, shows that a Dirac-like energy bands crossing is formed in the energy gap for spin-up states above the Fermi level at a binding energy  $E - E_F = +0.072$  eV. The orbital analysis of this state demonstrates the contribution of the graphene  $\pi$  character with the dominant contribution of the Ni  $3d$  states. Further analysis shows that the considered bands are not the result of band folding; obviously a deeper analysis of the nature of these states is necessary.

Finally, it is interesting to consider the calculated electronic structure for the sharp interface gr/1 ML-Mn/Ni(111) (Fig. 7(b)). For spin-down states, a very big  $n$ -doping of graphene is observed and the Dirac point in this case is located at  $E - E_F = -2.3$  eV. A similar situation is also found for the spin-up states although the structure of the Dirac point is less pronounced. This situation is not obvious for the case of graphene adsorption on a metal with a partially filled  $d$  shell (Mn has an electronic configuration  $3d^5 4s^2$ ). Here one can speculate that the half-filled  $3d$  orbital has an orbital moment of  $L = 0$  which leads to the spherical symmetry of atomic orbitals in Mn. Therefore Mn might behave like Ca donating electrons to graphene and producing a relatively large  $n$ -doping of the graphene layer at a very short distance of 2.04 Å between graphene and Mn. This property of the Mn-intercalated layer can be used in further experiments on intercalation of Mn layers underneath graphene where the formation of Mn-alloys can be avoided.

### III. CONCLUSIONS

The intercalation of Mn atoms in the gr/Ni(111) interface leads to the formation of a graphene-protected thin Ni<sub>3</sub>Mn layer as deduced from our experimental data. At the gr/Ni<sub>3</sub>Mn interface, the graphene layer exhibits a slightly reduced  $n$ -doping compared to the parent gr/Ni(111) system. All experimental results are analyzed in the framework of state-of-the-art DFT calculations, demonstrating very good agreement between all data. The observed effects are explained by the hybridization between the valence band states of graphene and the underlying strong FM Ni<sub>3</sub>Mn. Additionally, the electronic structures of different gr/Mn-Ni interfaces were analysed with DFT, and we conclude that a hypothetical sharp gr-Mn interface prepared on a substrate without alloying effects would lead to strongly  $n$ -doped graphene, which can be used in further studies of different physical phenomena in graphene-based low-dimensional systems.

## Experimental

All experiments were performed in several stations under identical experimental conditions allowing reproducibility of all results. We prepared gr/Ni(111) under UHV conditions following the procedure described in the literature: a pre-cleaned Ni(111) crystal was exposed to  $C_2H_4$  at  $600^\circ C$  and  $p = 1 \times 10^{-6}$  mbar for 15 min [30]. Manganese was evaporated from a carefully degassed  $e$ -beam source at a pressure below  $p = 5 \times 10^{-10}$  mbar and its thickness (slightly more than 1 ML) was measured with a quartz microbalance and then further estimated on the basis of spectroscopic experiments. Annealing of the Mn/gr/Ni(111) system at  $400^\circ C$  leads to the formation of the ordered gr/Ni<sub>3</sub>Mn interface. The ordering and cleanness of the system at every preparation step was verified with low-energy electron diffraction (LEED), scanning tunnelling microscopy (STM) and x-ray photoelectron spectroscopy (XPS).

Initial preparation/spectroscopic experiments were performed in the laboratory station equipped with a SPECS PHOIBOS 150 hemispherical analyzer and combined non-monochromotized AlK $\alpha$ /MgK $\alpha$  x-ray source. Further angle-resolved photoelectron spectroscopy (ARPES) experiments were performed at the UE 56/2-PGM beamline of the BESSY II storage ring (HZB Berlin). ARPES data were collected in the snapshot mode with a SPECS PHOIBOS 100 hemispherical analyzer equipped with the 2D-CCD detector while the sample was placed on a 5-axis fully-motorized manipulator. The sample was pre-aligned (via polar and azimuth angles rotations) in such a way that the tilt scan was performed along the  $\Gamma - K$  direction of the graphene-derived Brillouin zone (BZ) with the photoemission intensity on the channelplate images acquired along the direction perpendicular to  $\Gamma - K$ . The final 3D data set of the photoemission intensity as a function of kinetic energy and two emission angles,  $I(E_{kin}; angle1; angle2)$ , were then carefully analyzed. NEXAFS data were collected at the D1011 beamline of MAX-lab (Lund) in the partial and total electron yield modes (PEY and TEY).

STM experiments were performed in the lab-station equipped with a SPECS STM Aarhus 150. STM measurements were performed in constant current mode at room temperature using electrochemically etched polycrystalline tungsten tips cleaned in UHV via Ar<sup>+</sup> sputtering. The sign of the bias voltage corresponds to the voltage applied to the sample. Tunnelling current and voltage are labelled  $I_T$  and  $U_T$ , respectively. In this station the additional

XPS equipment (SPECS PHOIBOS 150 and SPECS monochromotized AlK $\alpha$ /AgL $\alpha$  x-ray source) was used for the control experiments during sample preparation.

DFT calculations based on plane-wave basis sets of 500 eV cutoff energy were performed with the Vienna *ab initio* simulation package (VASP) [48, 49]. The Perdew-Burke-Ernzerhof (PBE) exchange-correlation functional [50] was employed. The electron-ion interaction was described within the projector augmented wave (PAW) method [51] with C (2*s*, 2*p*), Ni (3*d*, 4*s*), Mn (3*d*, 4*s*) states treated as valence states. The BZ integration was performed on  $\Gamma$ -centred symmetry reduced Monkhorst-Pack meshes using a Methfessel-Paxton smearing method of first order with  $\sigma = 0.15$  eV, except for the calculation of total energies. For these calculations, the tetrahedron method with Blöchl corrections [52] was employed. The *k*-mesh for sampling of the supercell Brillouin zone was chosen to be as dense as  $24 \times 24$ , when folded up to the simple graphene unit cell. Dispersion interactions were considered adding a  $1/r^6$  atom-atom term as parameterised by Grimme (“D2” parameterisation) [53].

The studied systems are modelled using supercells which have a  $(2 \times 2)$  lateral periodicity with respect to graphene and contain 13 layers of metal atoms (4 atoms per layer), a graphene sheet (8 atoms per layer) adsorbed on both sides of the slab and a vacuum gap of approximately 23 Å. In the case of the graphene-Mn-Ni(111) system, an additional Mn-layer is added from both sides of the slab between graphene and Ni(111). During the structural optimisation the positions of the carbon atoms (*x,y,z*-coordinates) as well as those of the top three layers of metal atoms (*z*-coordinates) are relaxed until forces became smaller than  $0.02 \text{ eV \AA}^{-1}$ .

The band structures calculated for the studied systems were unfolded (if necessary) to the graphene  $(1 \times 1)$  primitive unit cells according to the procedure described in Ref. 54 and 55 with the code BandUP.

### **Acknowledgement**

The computing facilities of the Freie Universität Berlin (ZEDAT) and the North-German Supercomputing Alliance (HLRN) are acknowledged for computer time. Yi Cui is grateful to the support from Natural Science Foundation of Jiangsu Province (BK20170426). We

acknowledge Alexei Preobrajenski for his help during beamtime at MAX-lab.

---

- [1] Batzill, M. The Surface Science of Graphene: Metal Interfaces, CVD Synthesis, Nanoribbons, Chemical Modifications, and Defects. *Surf. Sci. Rep.* **2012**, *67*, 83–115.
- [2] Dedkov, Y.; Voloshina, E. Graphene Growth and Properties on Metal Substrates. *J. Phys.: Condens. Matter* **2015**, *27*, 303002.
- [3] Bae, S. et al. Roll-to-Roll Production of 30-Inch Graphene Films for Transparent Electrodes. *Nat. Nanotech.* **2010**, *5*, 574–578.
- [4] Liu, N.; Fu, L.; Dai, B.; Yan, K.; Liu, X.; Zhao, R.; Zhang, Y.; Liu, Z. Universal Segregation Growth Approach to Wafer-Size Graphene from Non-Noble Metals. *Nano Lett.* **2011**, *11*, 297–303.
- [5] Lee, H. C.; Liu, W.-W.; Chai, S.-P.; Mohamed, A. R.; Aziz, A.; Khe, C.-S.; Hidayah, N. M. S.; Hashim, U. Review of the Synthesis, Transfer, Characterization and Growth Mechanisms of Single and Multilayer Graphene. *RSC Adv.* **2017**, *7*, 15644–15693.
- [6] Kim, K. S.; Zhao, Y.; Jang, H.; Lee, S. Y.; Kim, J. M.; Kim, K. S.; Ahn, J.-H.; Kim, P.; Choi, J.-Y.; Hong, B. H. Large-Scale Pattern Growth of Graphene Films for Stretchable Transparent Electrodes. *Nature* **2009**, *457*, 706–710.
- [7] Ryu, J.; Kim, Y.; Won, D.; Kim, N.; Park, J. S.; Lee, E.-K.; Cho, D.; Cho, S.-P.; Kim, S. J.; Ryu, G. H.; Shin, H.-A.-S.; Lee, Z.; Hong, B. H.; Cho, S. Fast Synthesis of High-Performance Graphene Films by Hydrogen-Free Rapid Thermal Chemical Vapor Deposition. *ACS Nano* **2014**, *8*, 950–956.
- [8] Dedkov, Y. S.; Fonin, M.; Laubschat, C. A Possible Source of Spin-Polarized Electrons: The Inert Graphene/Ni(111) system. *Appl. Phys. Lett.* **2008**, *92*, 052506.
- [9] Dedkov, Y. S.; Fonin, M.; Ruediger, U.; Laubschat, C. Graphene-Protected Iron Layer on Ni(111). *Appl. Phys. Lett.* **2008**, *93*, 022509.
- [10] Sutter, E.; Albrecht, P.; Camino, F. E.; Sutter, P. Monolayer Graphene as Ultimate Chemical Passivation Layer for Arbitrarily Shaped Metal Surfaces. *Carbon* **2010**, *48*, 4414–4420.
- [11] Weatherup, R. S.; D’Arsie, L.; Cabrero-Vilatela, A.; Caneva, S.; Blume, R.; Robertson, J.; Schloegl, R.; Hofmann, S. Long-Term Passivation of Strongly Interacting Metals with Single-Layer Graphene. *J. Am. Chem. Soc.* **2015**, *137*, 14358–14366.

- [12] Campbell, G. P.; Kiraly, B.; Jacobberger, R. M.; Mannix, A. J.; Arnold, M. S.; Hersam, M. C.; Guisinger, N. P.; Bedzyk, M. J. Epitaxial Graphene-Encapsulated Surface Reconstruction of Ge(110). *Phys. Rev. Mater.* **2018**, *2*, 044004.
- [13] Tesch, J.; Paschke, F.; Fonin, M.; Wietstruk, M.; Böttcher, S.; Koch, R. J.; Bostwick, A.; Jozwiak, C.; Rotenberg, E.; Makarova, A.; Paulus, B.; Voloshina, E.; Dedkov, Y. The Graphene/n-Ge(110) Interface: Structure, Doping, and Electronic Properties. *Nanoscale* **2018**, *10*, 6088–6098.
- [14] Zhou, D.; Niu, Z.; Niu, T. Surface Reconstruction of Germanium: Hydrogen Intercalation and Graphene Protection. *J. Phys. Chem. C* **2018**, *122*, 21874–21882.
- [15] Voloshina, E.; Dedkov, Y. Graphene on Metallic Surfaces: Problems and Perspectives. *Phys. Chem. Chem. Phys.* **2012**, *14*, 13502–13514.
- [16] Voloshina, E. N.; Dedkov, Y. S. General Approach to Understanding the Electronic Structure of Graphene on Metals. *Mater. Res. Express* **2014**, *1*, 035603.
- [17] Karpan, V. M.; Giovannetti, G.; Khomyakov, P. A.; Talanana, M.; Starikov, A. A.; Zwierzycki, M.; Brink, J. v. d.; Brocks, G.; Kelly, P. J. Graphite and Graphene as Perfect Spin Filters. *Phys. Rev. Lett.* **2007**, *99*, 176602.
- [18] Karpan, V. M.; Khomyakov, P. A.; Starikov, A. A.; Giovannetti, G.; Zwierzycki, M.; Talanana, M.; Brocks, G.; Brink, J. v. d.; Kelly, P. J. Theoretical Prediction of Perfect Spin Filtering at Interfaces Between Close-Packed Surfaces of Ni or Co and Graphite or Graphene. *Phys. Rev. B* **2008**, *78*, 195419.
- [19] Karpan, V.; Khomyakov, P.; Giovannetti, G.; Starikov, A.; Kelly, P. Ni(111)—graphene—h-BN Junctions as Ideal Spin Injectors. *Phys. Rev. B* **2011**, *84*.
- [20] Weser, M.; Rehder, Y.; Horn, K.; Sicot, M.; Fonin, M.; Preobrajenski, A. B.; Voloshina, E. N.; Goering, E.; Dedkov, Y. S. Induced Magnetism of Carbon Atoms at the Graphene/Ni(111) Interface. *Appl. Phys. Lett.* **2010**, *96*, 012504.
- [21] Dedkov, Y. S.; Fonin, M. Electronic and Magnetic Properties of the Graphene-Ferromagnet Interface. *New J. Phys.* **2010**, *12*, 125004.
- [22] Weser, M.; Voloshina, E. N.; Horn, K.; Dedkov, Y. S. Electronic Structure and Magnetic Properties of the Graphene/Fe/Ni(111) Intercalation-Like System. *Phys. Chem. Chem. Phys.* **2011**, *13*, 7534–7539.
- [23] Marchenko, D.; Varykhalov, A.; Sanchez-Barriga, J.; Rader, O.; Carbone, C.; Bihlmayer, G.

- Highly Spin-Polarized Dirac Fermions at the Graphene/Co Interface. *Phys. Rev. B* **2015**, *91*, 235431.
- [24] Usachov, D.; Fedorov, A.; Otrokov, M. M.; Chikina, A.; Vilkov, O.; Petukhov, A.; Rybkin, A. G.; Koroteev, Y. M.; Chulkov, E. V.; Adamchuk, V. K.; Grüneis, A.; Laubschat, C.; Vyalikh, D. V. Observation of Single-Spin Dirac Fermions at the Graphene/ Ferromagnet Interface. *Nano Lett.* **2015**, *15*, 2396–2401.
- [25] Dedkov, Y. S.; Shikin, A. M.; Adamchuk, V. K.; Molodtsov, S. L.; Laubschat, C.; Bauer, A.; Kaindl, G. Intercalation of Copper Underneath a Monolayer of Graphite on Ni(111). *Phys. Rev. B* **2001**, *64*, 035405.
- [26] Varykhalov, A.; Sanchez-Barriga, J.; Shikin, A. M.; Biswas, C.; Vescovo, E.; Rybkin, A.; Marchenko, D.; Rader, O. Electronic and Magnetic Properties of Quasifreestanding Graphene on Ni. *Phys. Rev. Lett.* **2008**, *101*, 157601.
- [27] Varykhalov, A.; Scholz, M.; Kim, T.; Rader, O. Effect of Noble-Metal Contacts on Doping and Band Gap of Graphene. *Phys. Rev. B* **2010**, *82*, 121101.
- [28] Voloshina, E. N.; Generalov, A.; Weser, M.; Böttcher, S.; Horn, K.; Dedkov, Y. S. Structural and Electronic Properties of the Graphene/Al/Ni(111) Intercalation System. *New J. Phys.* **2011**, *13*, 113028.
- [29] Omiciuolo, L.; ndez, E. R. H. a.; Miniussi, E.; Orlando, F.; Lacovig, P.; Lizzit, S.; scedil, T. O. M.; Locatelli, A.; Larciprete, R.; Bianchi, M.; Ulstrup, S. o. r.; Hofmann, P.; egrave, D. A.; Baraldi, A. Bottom-Up Approach for the Low-Cost Synthesis of Graphene-Alumina Nanosheet Interfaces Using Bimetallic Alloys. *Nat. Commun.* **2014**, *5*, 5062.
- [30] Dedkov, Y.; Klesse, W.; Becker, A.; Späth, F.; Papp, C.; Voloshina, E. Decoupling of Graphene from Ni(111) via Formation of an Interfacial NiO Layer. *Carbon* **2017**, *121*, 10–16.
- [31] Larciprete, R.; Colonna, S.; Ronci, F.; Flammini, R.; Lacovig, P.; Apostol, N.; Politano, A.; Feulner, P.; Menzel, D.; Lizzit, S. Self-Assembly of Graphene Nanoblister Sealed to a Bare Metal Surface. *Nano Lett.* **2016**, *16*, 1808–1817.
- [32] Bignardi, L.; Lacovig, P.; Dalmiglio, M. M.; Orlando, F.; Ghafari, A.; Petaccia, L.; Baraldi, A.; Larciprete, R.; Lizzit, S. Key Role of Rotated Domains in Oxygen Intercalation at Graphene on Ni(111). *2D Materials* **2017**, *4*, 025106.
- [33] Schröder, U. A.; Petrovic, M.; Gerber, T.; Martinez-Galera, A. J.; Grånäs, E.; Arman, M. A.; Herbig, C.; Schnadt, J.; Kralj, M.; Knudsen, J.; Michely, T. Core Level Shifts of Intercalated

- Graphene. *2D Materials* **2017**, *4*, 015013.
- [34] Dürr, H. A.; van der Laan, G.; Spanke, D.; Hillebrecht, F. U.; Brookes, N. B. Electron-Correlation-Induced Magnetic Order of Ultrathin Mn Films. *Phys. Rev. B* **1997**, *56*, 8156–8162.
- [35] Allen, M.; Venus, D. Ordered Alloy Films of Ni and Mn Grown on Ni(111)/W(110). *Surf. Sci.* **2001**, *477*, 209–218.
- [36] Rader, O.; Mizokawa, T.; Fujimori, A.; Kimura, A. Structure and Electron Correlation of Mn on Ni(110). *Phys. Rev. B* **2001**, *64*, 165414.
- [37] Manju, U.; Topwal, D.; Rossi, G.; Vobornik, I. Electronic Structure of the Two-Dimensionally Ordered Mn/Cu(110) Magnetic Surface Alloy. *Phys. Rev. B* **2010**, *82*, 035442.
- [38] Voloshina, E.; Ovcharenko, R.; Shulakov, A.; Dedkov, Y. Theoretical Description of X-ray Absorption Spectroscopy of the Graphene-Metal Interfaces. *J. Chem. Phys.* **2013**, *138*, 154706.
- [39] Matsumoto, Y.; Entani, S.; Koide, A.; Ohtomo, M.; Avramov, P. V.; Naramoto, H.; Amemiya, K.; Fujikawa, T.; Sakai, S. Spin Orientation Transition Across the Single-Layer Graphene/Nickel Thin Film Interface. *J. Mater. Chem. C* **2013**, *1*, 5533–5537.
- [40] Verbitskiy, N. I.; Fedorov, A. V.; Profeta, G.; Stroppa, A.; Petaccia, L.; Senkovskiy, B.; Nefedov, A.; Wöll, C.; Usachov, D. Y.; Vyalikh, D. V.; Yashina, L. V.; Eliseev, A. A.; Pichler, T.; Grüneis, A. Atomically Precise Semiconductor-Graphene and hBN Interfaces by Ge Intercalation. *Sci. Rep.* **2015**, *5*, 17700.
- [41] Bertoni, G.; Calmels, L.; Altibelli, A.; Serin, V. First-Principles Calculation of the Electronic Structure and EELS Spectra at the Graphene/Ni(111) Interface. *Phys. Rev. B* **2004**, *71*, 075402.
- [42] Achilli, S.; Tognolini, S.; Fava, E.; Ponzoni, S.; Drera, G.; Cepek, C.; Patera, L. L.; Africh, C.; Castillo, E. d.; Trioni, M. I.; Pagliara, S. Surface States Characterization in the Strongly Interacting Graphene/Ni(111) System. *New J. Phys.* **2018**, *20*, 103039.
- [43] Kreutz, T. J.; Greber, T.; Aebi, P.; Osterwalder, J. Temperature-Dependent Electronic Structure of Nickel Metal. *Phys. Rev. B* **1998**, *58*, 1300–1317.
- [44] Mulazzi, M.; Hochstrasser, M.; Corso, M.; Vobornik, I.; Fujii, J.; Osterwalder, J.; Henk, J.; Rossi, G. Matrix Element Effects in Angle-Resolved Valence Band Photoemission with Polarized Light from the Ni(111) Surface. *Phys. Rev. B* **2006**, *74*, 035118.
- [45] Kulkova, S. E.; Valujsky, D. V.; Kim, J.-S.; Lee, G.; Koo, Y. M. The Electronic Properties of

- FeCo, Ni<sub>3</sub>Mn and Ni<sub>3</sub>Fe at the Order-Disorder Transition. *Physica B*, **2002**, *322*, 236–247.
- [46] Palumbo, M.; Fries, S. G.; Corso, A. D.; Körmann, F.; Hickel, T.; Neugebauer, J. Reliability Evaluation of Thermophysical Properties from First-Principles Calculations. *J. Phys.: Condens. Matter* **2014**, *26*, 335401.
- [47] Tian, D.; Li, H.; Wu, S. C.; Jona, F.; Marcus, P. M. Atomic and Electronic Structure of Thin Films of Mn on Pd{111}. *Phys. Rev. B* **1992**, *45*, 3749–3754.
- [48] Kresse, G.; Hafner, J. Norm-Conserving and Ultrasoft Pseudopotentials for First-Row and Transition Elements. *J. Phys.: Condens. Matter* **1994**, *6*, 8245–8257.
- [49] Kresse, G.; Furthmüller, J. Efficiency of Ab-Initio Total Energy Calculations for Metals and Semiconductors Using a Plane-Wave Basis Set. *Comp. Mater. Sci.* **1996**, *6*, 15–50.
- [50] Perdew, J.; Burke, K.; Ernzerhof, M. Generalized Gradient Approximation Made Simple. *Phys. Rev. Lett.* **1996**, *77*, 3865–3868.
- [51] Blöchl, P. E. Projector Augmented-Wave Method. *Phys. Rev. B* **1994**, *50*, 17953–17979.
- [52] Blöchl, P. E.; Jepsen, O.; Andersen, O. Improved Tetrahedron Method for Brillouin-Zone Integrations. *Phys. Rev. B* **1994**, *49*, 16223–16233.
- [53] Grimme, S. Semiempirical GGA-Type Density Functional Constructed with a Long-Range Dispersion Correction. *J. Comput. Chem.* **2006**, *27*, 1787–1799.
- [54] Medeiros, P. V. C.; Stafström, S.; Björk, J. Effects of Extrinsic and Intrinsic Perturbations on the Electronic Structure of Graphene: Retaining an Effective Primitive Cell Band Structure by Band Unfolding. *Phys. Rev. B* **2014**, *89*, 041407.
- [55] Medeiros, P. V. C.; Tsirkin, S. S.; Stafström, S.; Björk, J. Unfolding Spinor Wave Functions and Expectation Values of General Operators: Introducing the Unfolding-Density Operator. *Phys. Rev. B* **2015**, *91*, 041116–5.

TABLE I: The interface carbon spin magnetic moments (in  $\mu_B$ ) as computed for the atoms marked in Figure 5.

System	C1	C2	C3	C4
(a) gr/Ni(111)	-0.019	0.034	-0.019	0.034
(b) gr/Mn/Ni(111)	-0.018	-0.018	-0.029	-0.029
(c) gr/Ni <sub>3</sub> Mn/Ni(111)	-0.047	0.021	0.050	0.021
(d) gr/Ni <sub>3</sub> Mn(111)	-0.051	0.023	0.037	0.023

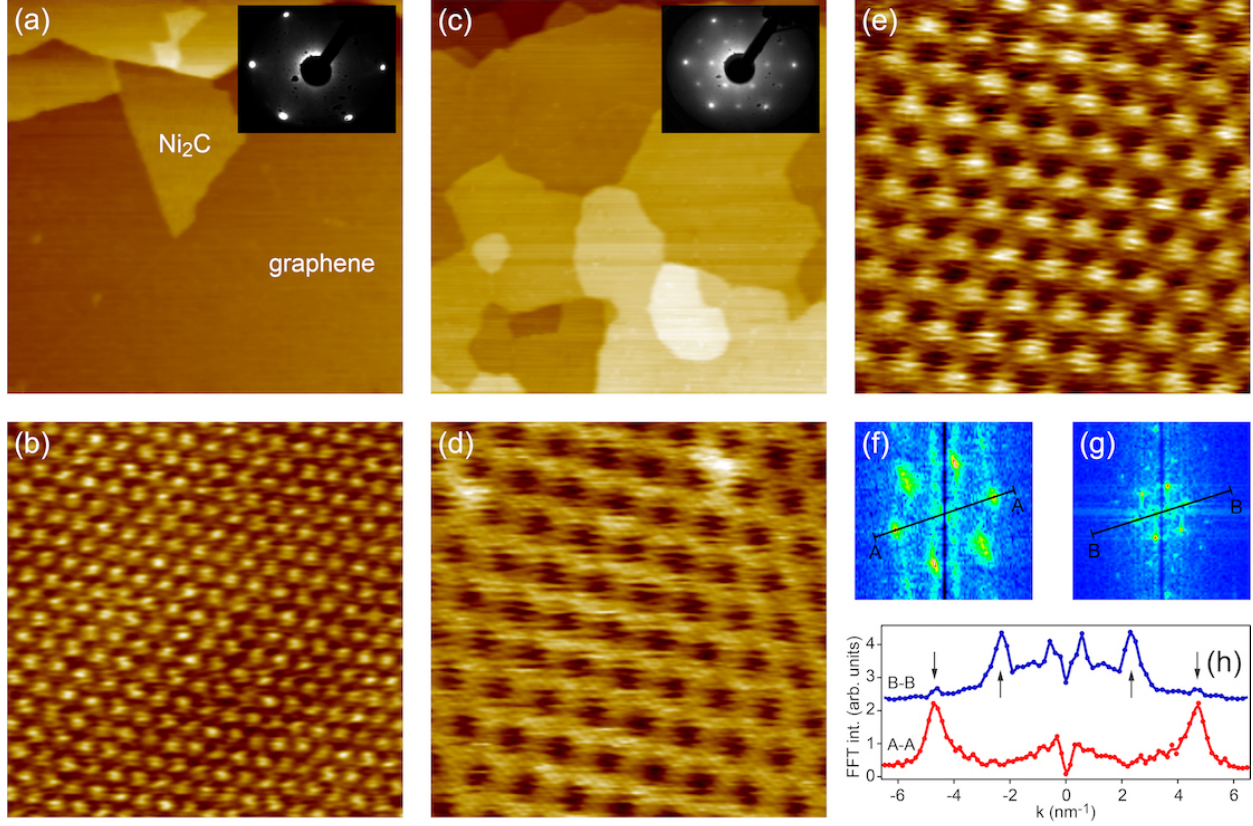


FIG. 1: (a,b) STM images of gr/Ni(111); scanning parameters: (a)  $150\text{nm} \times 150\text{nm}$ ,  $U_T = +0.1\text{ V}$ ,  $I_T = 0.31\text{ nA}$ , (b)  $4\text{nm} \times 4\text{nm}$ ,  $U_T = +0.005\text{ V}$ ,  $I_T = 0.52\text{ nA}$ . (c-e) STM images of the system obtained after intercalation of Mn in gr/Ni(111); scanning parameters: (c)  $135\text{nm} \times 135\text{nm}$ ,  $U_T = +1.25\text{ V}$ ,  $I_T = 0.1\text{ nA}$ , (d)  $4\text{nm} \times 4\text{nm}$ ,  $U_T = +0.022\text{ V}$ ,  $I_T = 0.11\text{ nA}$ , (e)  $4\text{nm} \times 4\text{nm}$ ,  $U_T = +0.01\text{ V}$ ,  $I_T = 0.31\text{ nA}$ . Insets of (a) and (c) show the respective LEED images collected at 80 eV and 110 eV. (f,g) FFT images of (b,e), respectively. (h) FFT intensity profiles taken in (f) and (g) with down- and up-arrows marking  $(1 \times 1)$  and  $(2 \times 2)$  periodicities, respectively.

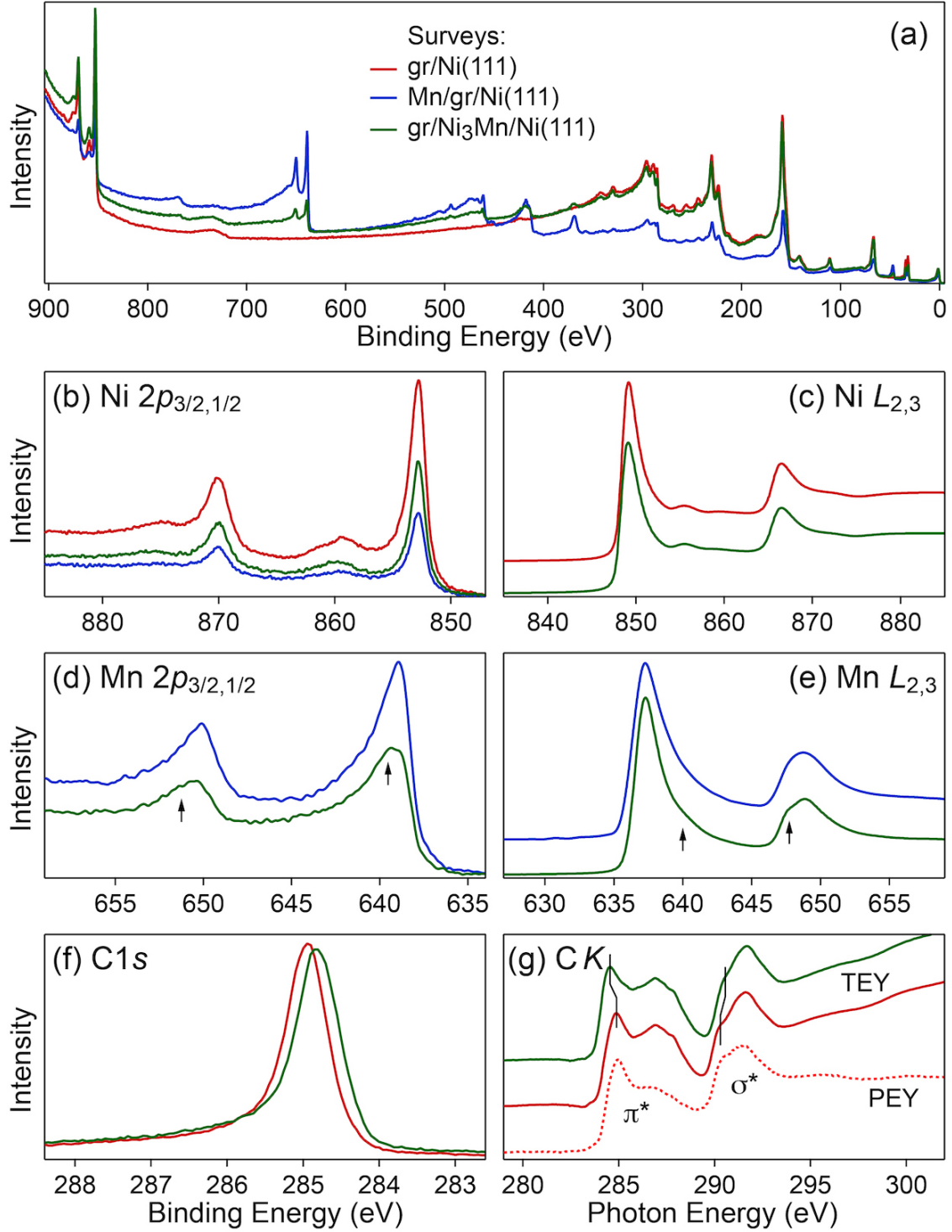


FIG. 2: XPS and NEXAFS spectra for systems under study: (a) XPS surveys, (b) XPS Ni  $2p_{3/2,1/2}$ , (c) NEXAFS Ni  $L_{2,3}$ , (d) XPS Mn  $2p_{3/2,1/2}$ , (e) NEXAFS Mn  $L_{2,3}$ , (f) XPS C  $1s$ , and (g) NEXAFS C  $K$ . Red, blue, and green colours shows spectra for gr/Ni(111), Mn/gr/Ni(111), and gr/Ni<sub>3</sub>Mn/Ni(111), respectively.

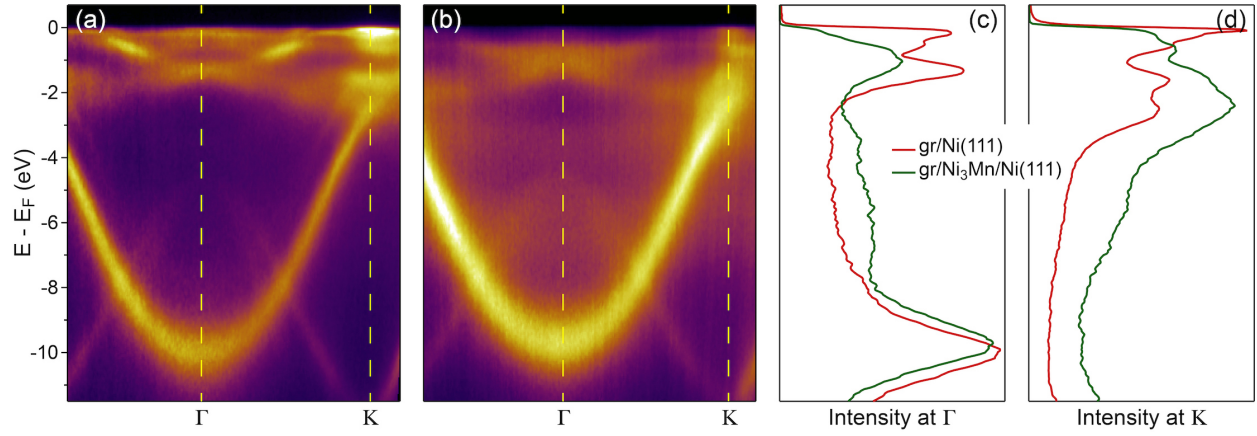


FIG. 3: ARPES intensity maps along  $\Gamma - K$  for (a) gr/Ni(111) and (b) gr/Ni<sub>3</sub>Mn/Ni(111). Photon energy used in the experiment is  $h\nu = 63$  eV. Intensity profiles extracted at the  $\Gamma$  and K points for both systems are shown in (c) and (d), respectively.

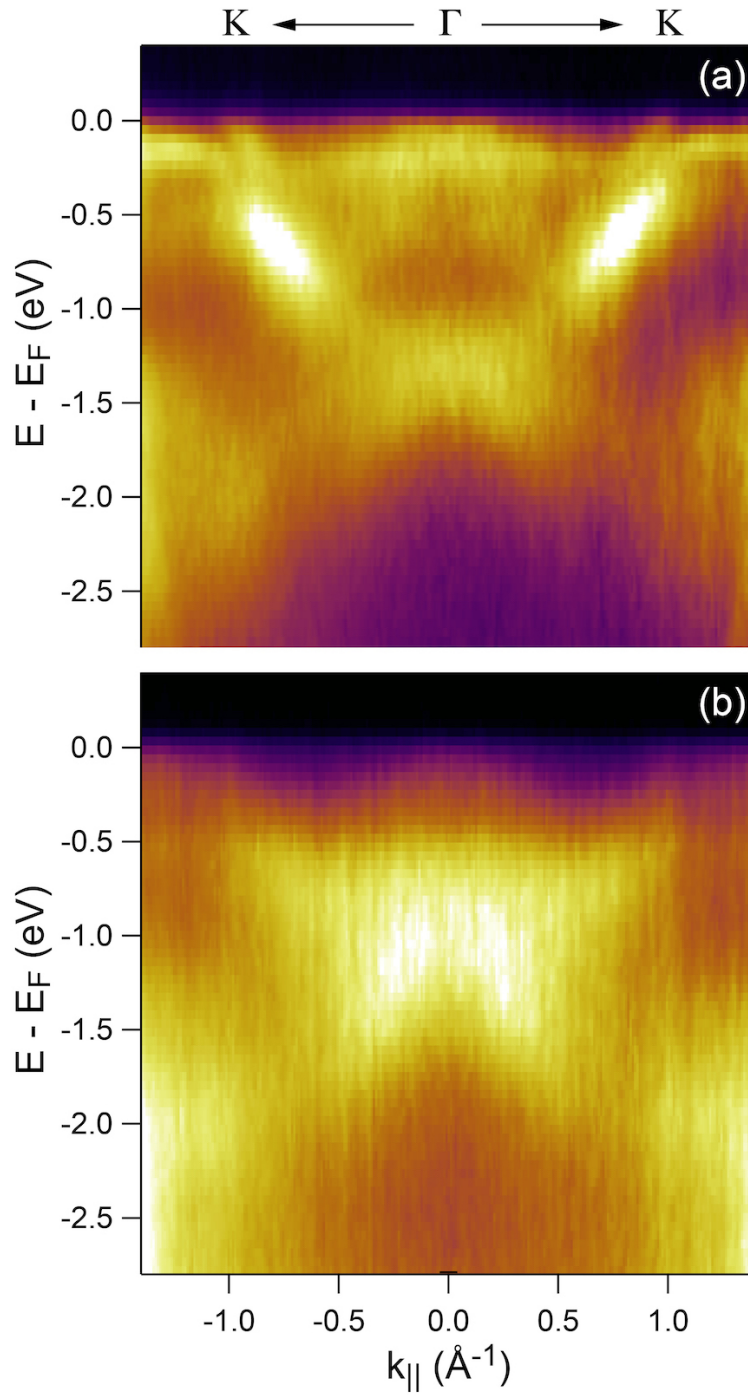


FIG. 4: ARPES intensity maps zoomed around the  $\Gamma$  point and  $E_F$  for (a) gr/Ni(111) and (b) gr/Ni<sub>3</sub>Mn/Ni(111).

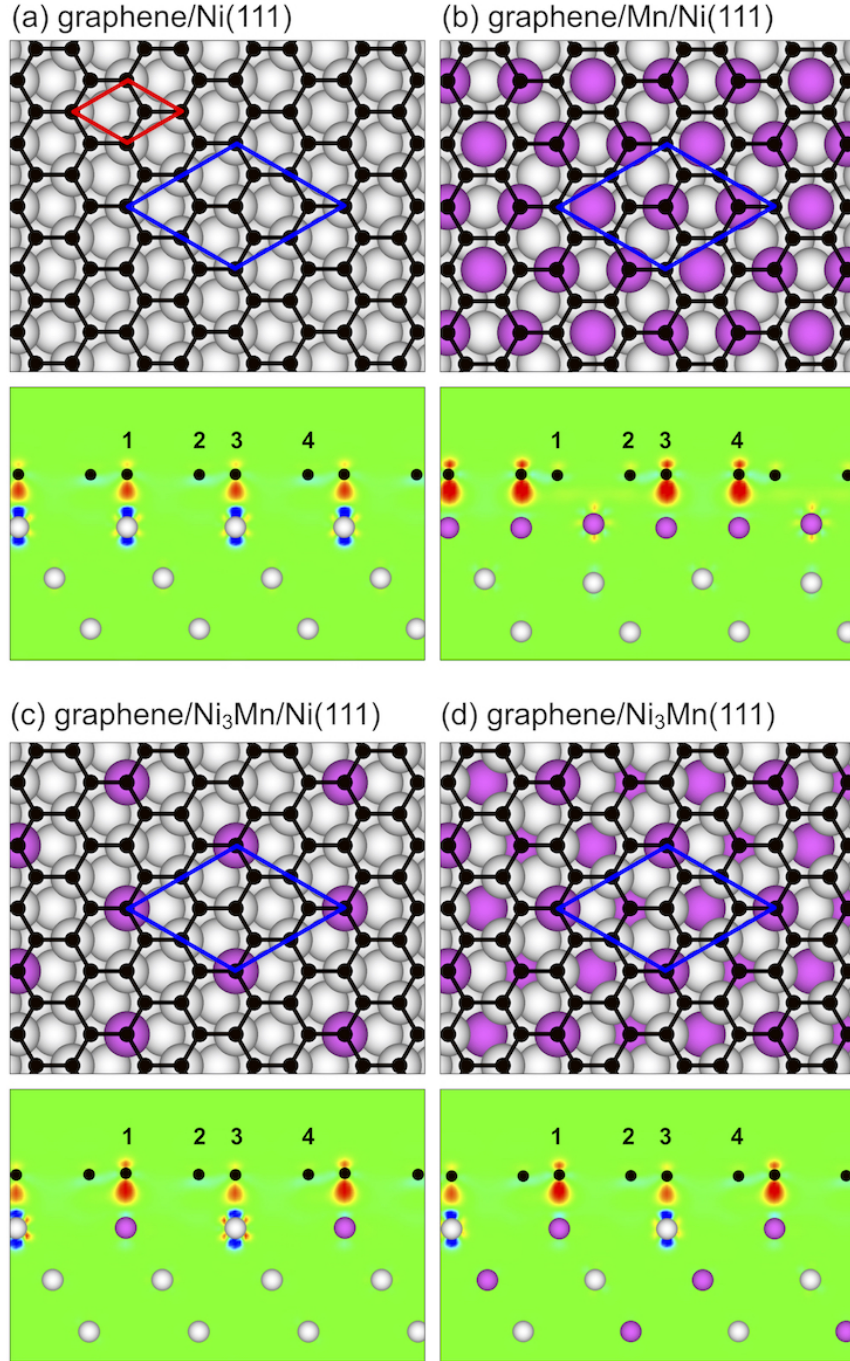


FIG. 5: Top and side views of different Mn-based intercalation structures: (a) parent gr/Ni(111), (b) gr/1 ML-Mn/Ni(111), (c) gr/1 ML-Ni<sub>3</sub>Mn/Ni(111), (d) gr/bulk-Ni<sub>3</sub>Mn(111). Side views for all structures are taken along the main diagonal of the big rhombus marked in the top views and they are overlaid with electron charge difference maps  $\Delta\rho(r) = \rho_{gr/s} - \rho_{gr} - \rho_s$  ( $s$  - substrate).  $\Delta\rho$  is colour coded as red ( $+0.02e/\text{\AA}^3$ ) – green (0) – blue ( $-0.02e/\text{\AA}^3$ ).

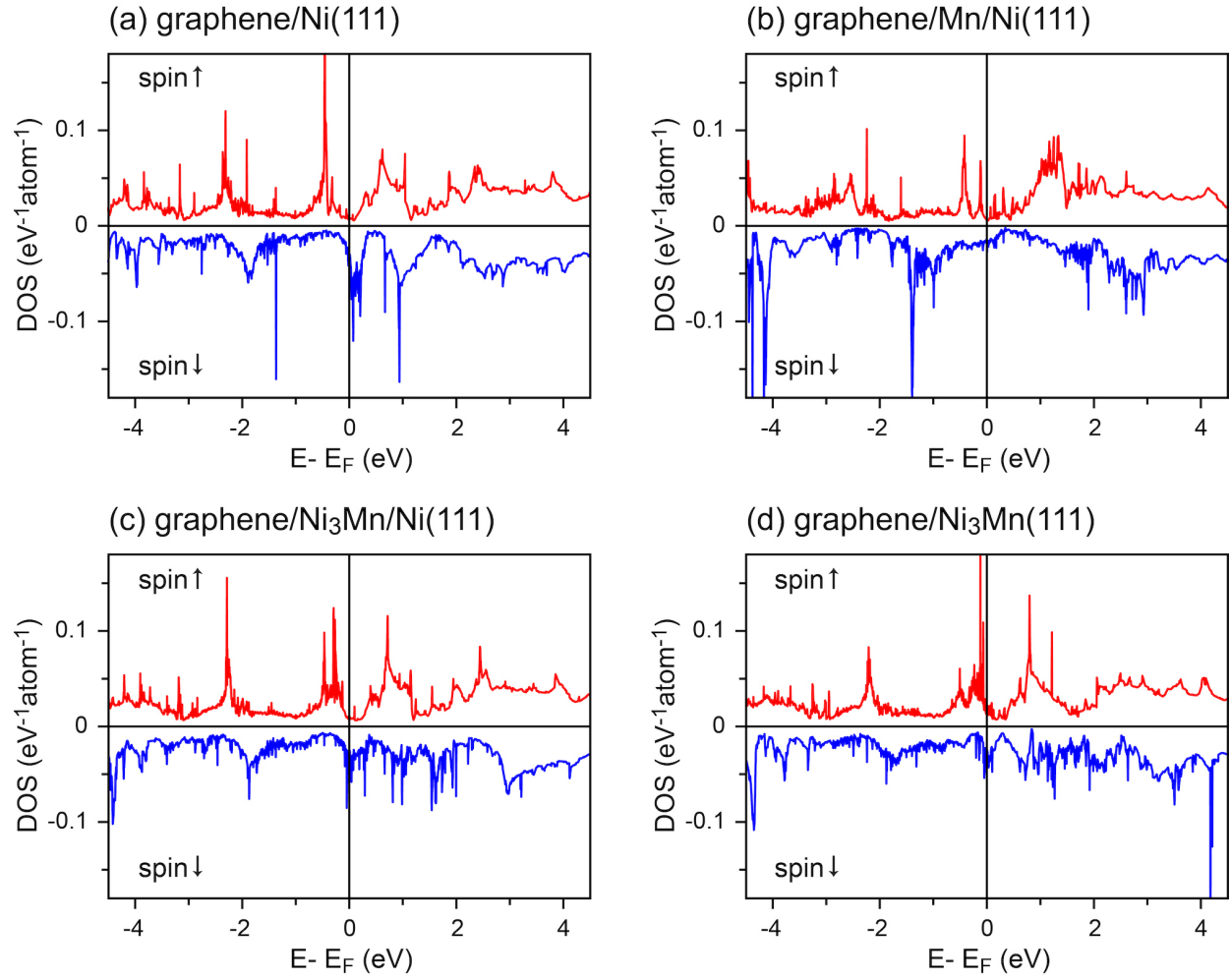


FIG. 6: Spin-resolved  $C$ - $p_z$ -projected density of states for (a) gr/Ni(111), (b) gr/1 ML-Mn/Ni(111), (c) gr/1 ML-Ni<sub>3</sub>Mn/Ni(111), and (d) gr/bulk-Ni<sub>3</sub>Mn(111).

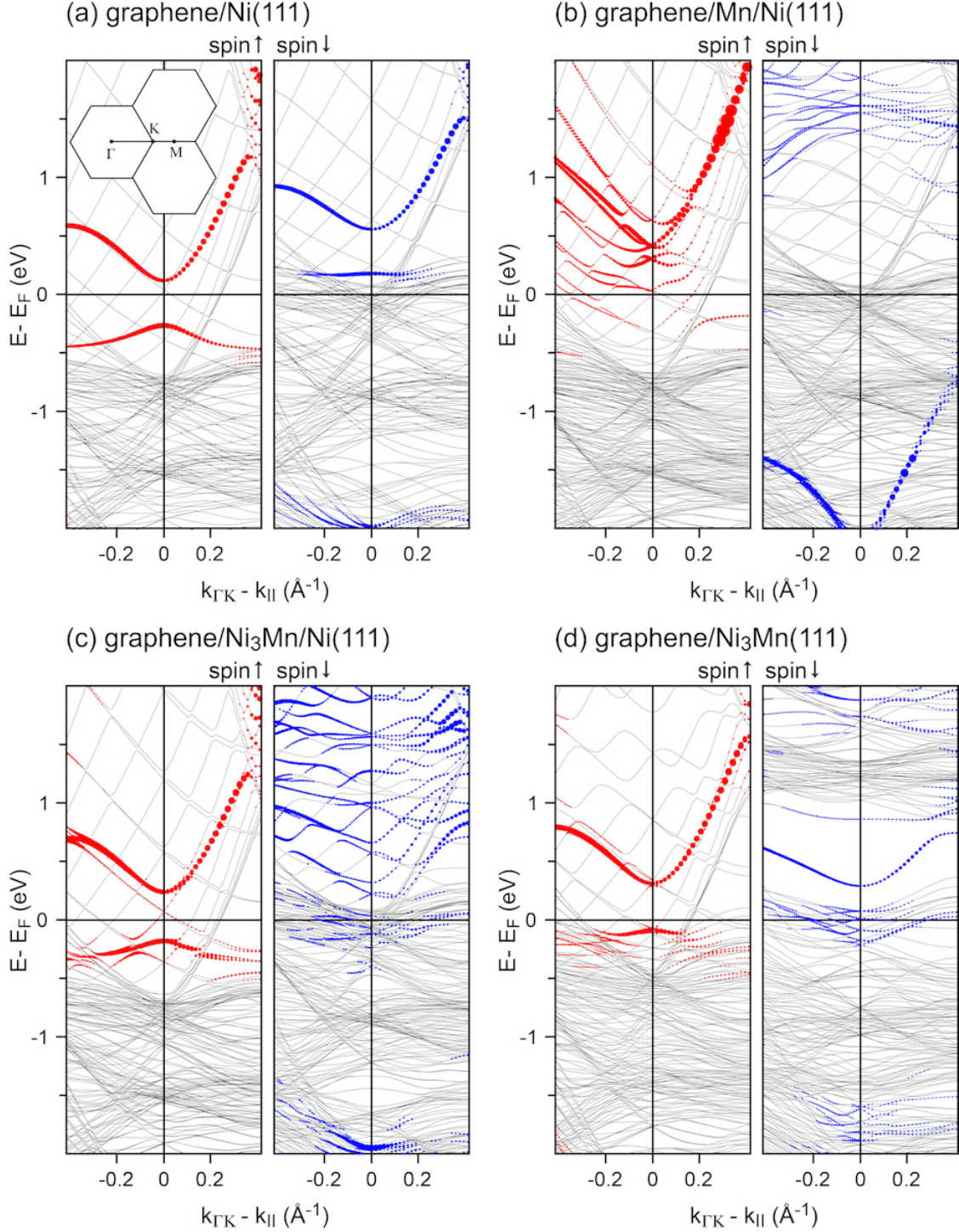


FIG. 7: Spin-resolved band structures for (a) gr/Ni(111), (b) gr/1 ML-Mn/Ni(111), (c) gr/1 ML-Ni<sub>3</sub>Mn/Ni(111), and (d) gr/bulk-Ni<sub>3</sub>Mn(111). Band structures are presented around  $\Gamma$  point for the graphene derived  $(1 \times 1)$  Brillouin zone. The weight of the graphene-derived  $p_z$  character is highlighted by the size of filled circles superimposed with the plot of the band structure.

